



Cite this: *J. Mater. Chem. A*, 2016, **4**,  
6006

## Porous nanoMoC@graphite shell derived from a MOFs-directed strategy: an efficient electrocatalyst for the hydrogen evolution reaction†

Zhangping Shi,<sup>a</sup> Yangxia Wang,<sup>a</sup> Huanlei Lin,<sup>b</sup> Hongbin Zhang,<sup>a</sup> Meikun Shen,<sup>a</sup> Songhai Xie,<sup>a</sup> Yahong Zhang,<sup>a</sup> Qingsheng Gao<sup>\*b</sup> and Yi Tang<sup>\*a</sup>

The hydrogen evolution reaction using noble-metal free electrocatalysts has captured increasing attention due to its importance in renewable hydrogen production. Herein, a highly active and stable electrocatalyst of MoC encapsulated by graphitized carbon shells (nanoMoC@GS) has been developed *via* an *in situ* carburization of a Mo-based metal–organic framework (Mo-MOF) with the atomic periodic structure. The ultrafine MoC nanoparticles ( $\sim 3$  nm) confined by 1–3 layered graphite shells significantly favor the efficient HER in both acidic and basic media. In particular, a low overpotential ( $\eta_{10} = 124$  and 77 mV at a current density of  $-10 \text{ mA cm}^{-2}$ ), a small Tafel slope (43 and 50 mV dec $^{-1}$ ) and a high exchange current density ( $j_0 = 0.015$  and  $0.212 \text{ mA cm}^{-2}$ ) are achieved on nanoMoC@GS in 0.5 M  $\text{H}_2\text{SO}_4$  and 1.0 M KOH, respectively. Such remarkable activity, outperforming most current noble-metal-free electrocatalysts, stems from the cooperative/synergistic effects of ultrafine MoC nanostructure, ultrathin and conductive graphitized carbon shells, and enriched porosity. This work demonstrates a feasible way to design high-performance electrocatalysts *via* converting “atomic contact” hybrid structures (e.g., MOFs), illustrating a new perspective for developing nanocatalysts in the energy chemistry field.

Received 4th March 2016  
Accepted 17th March 2016

DOI: 10.1039/c6ta01900e  
[www.rsc.org/MaterialsA](http://www.rsc.org/MaterialsA)

### Introduction

Owing to soaring global energy consumption and serious environmental issues, renewable energy sources are the focus of much research and development worldwide. Hydrogen is regarded as a promising alternative to traditional fossil fuels because of its renewable nature, environment-friendly properties, and high energy density, especially when obtained from water electrolysis rather than coal and hydrocarbons (e.g., by well-assessed steam-reforming methods).<sup>1,2</sup> Recently, the hydrogen evolution reaction (HER) by water electrolysis has attracted great interest, which is promising for hydrogen production *via* the use of renewable electric energy.<sup>3–5</sup> In this process, the electrocatalyst is the crucial issue, which must be capable of lowering electrochemical overpotential with high

stability.<sup>3</sup> Although platinum group materials have proven to be the most efficient HER electrocatalysts, high cost and scarcity limit their large-scale applications. Hence, in recent years, two approaches have been adopted to optimize this process: (1) improving the catalytic performance of Pt-based catalysts *via* nanoengineering strategies,<sup>6,7</sup> and (2) developing low-cost alternatives for noble-metal HER catalysts.<sup>5,8–11</sup>

Recent studies have shown that transition metal carbides, such as molybdenum carbides, are promising electrocatalysts for HER because of their similar electronic and catalytic properties to Pt-group metals.<sup>12–14</sup> For those catalysts, abundant porosity,<sup>13,15</sup> nanostructure<sup>13,16</sup> and introduction of doping elements and conductive supports<sup>17–20</sup> are important in optimizing their HER performance, all of which have been the focus of research in recent years. To date, the controllable preparation of nanostructured metal carbides with high specific surface area and large pore volume still remains a great challenge, because a high reaction temperature tends to be used in the synthesis process. Hence, new synthesis methods are continually being developed to solve this conundrum, such as solid-phase synthesis,<sup>14,20–22</sup> and *in situ* carburization of molybdenum salt supported on carbon materials.<sup>16,23</sup> In our previous research, nanoporous Mo<sub>2</sub>C nanowires were developed through simply carburizing the  $\text{Mo}_3\text{O}_{10}(\text{C}_6\text{H}_8\text{N}) \cdot 2\text{H}_2\text{O}$  precursor under an inert atmosphere, and good HER performance was achieved on this

<sup>a</sup>Department of Chemistry, Shanghai Key Laboratory of Molecular Catalysis and Innovative Materials, Laboratory of Advanced Materials and Collaborative Innovation Center of Chemistry for Energy Materials, Fudan University, No. 220 Handan Road, 200433 Shanghai, P. R. China. E-mail: [yitang@fudan.edu.cn](mailto:yitang@fudan.edu.cn)

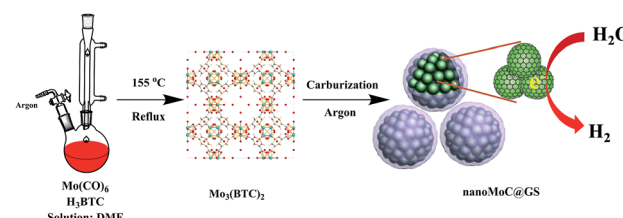
<sup>b</sup>Department of Chemistry, Jinan University, No. 601 Huangpu Avenue West, 510632 Guangzhou, P. R. China. E-mail: [tqsgao@jnu.edu.cn](mailto:tqsgao@jnu.edu.cn)

† Electronic supplementary information (ESI) available: Additional XRD, FESEM, TEM, HRTEM, XPS spectra, electrochemical characterization of nanoMoC@GS(T), and comparison of HER performance with other electrocatalysts. See DOI: [10.1039/c6ta01900e](https://doi.org/10.1039/c6ta01900e)

material.<sup>13</sup> These organic–inorganic hybrid nanowires developed by our group can provide the “sub-nanometer contact” between  $\text{Mo}_3\text{O}_{10}^{2-}$  and protonated aniline and create a quasi-homogeneous reaction environment for the carburization,<sup>24,25</sup> which favors formation of the nanoporous and nanostructured  $\text{Mo}_2\text{C}$ . However, the  $\text{Mo}_2\text{C}$  electrocatalyst synthesized by this method often possessed a relatively large particle-size (10–15 nm), as well as deficient conductive carbon species after carburization, which might prohibit the exposure of active  $\text{Mo}_2\text{C}$  sites and slow the charge transfer kinetics during the HER process. Recently, we successfully developed heteronanowires of  $\text{MoC}$ – $\text{Mo}_2\text{C}$  with varying  $\text{MoC}/\text{Mo}_2\text{C}$  by the same strategy,<sup>26</sup> and successfully improved the HER performance from our previous work on nanoporous  $\text{Mo}_2\text{C}$  by effective electron regulation. In addition, similar strategies were also widely adopted to develop other electrocatalysts for different electrochemical processes, such as ORR.<sup>27–30</sup> However, the deficiency of close and ordered contacts of metal atoms and organics in the precursors led to electrocatalyst processing of larger particle sizes and uneven dispersion of the supported active sizes after pyrolysis.

Metal–organic frameworks (MOFs) comprise a new class of porous and organic–inorganic hybrid materials with broad-based direct applications.<sup>31,32</sup> Moreover, these materials possess abundant organic ligands and atomic periodic structure, which can offer unique benefits for “atomic contact” between the metal ions and organic ligands. Such special features of MOFs make them possible precursors or templates for the fabrication of porous and nanostructured materials, such as porous carbon, metal oxides and metal oxide/carbon.<sup>33–36</sup> To date, only Lou and colleagues' group have creatively developed a “MOFs-assisted strategy” to synthesize porous molybdenum carbide.<sup>15</sup> In this strategy, a Cu-based MOF was used as the template, and the  $\text{MoC}_x$ –Cu composite material was prepared by carburization reactions between the organic ligands and guest polyoxometalates (POMs) that pre-embed in the pores of the MOF host. The porous  $\text{MoC}_x$  electrocatalyst was finally obtained after removing metallic Cu particles *via*  $\text{Fe}^{3+}$  etching, and exhibited good HER performance.  $\text{MoC}_x$  species have usually been proven to oxidize on the surface even in ambient conditions;<sup>12,22,37</sup> the etching operation *via* oxidative  $\text{Fe}^{3+}$  ions should be avoided if possible. Additionally, using Cu-MOF as a template and carburizing the organic ligand with the supported POMs in the pores is not beneficial for real “atomic contact” between the Mo ions and organic ligand, which might not favor the formation of uniform  $\text{MoC}_x$  nanostructures.<sup>15</sup> Hence, we predicted that ultrafine and porous  $\text{MoC}_x$  nanoparticles would likely be generated *via* the simple *in situ* carburizing of Mo-based MOF (Mo-MOF). The introduced carbon species derived from the sufficient organic ligands in MOF would confine and stabilize the  $\text{MoC}_x$  nanocrystallites during the carburization process, and accelerate the charge transfer kinetics in the electrochemical process due to excellent conductivity.

Herein, we developed a “MOFs-directed strategy” for synthesizing porous and uniformly nanostructured  $\text{MoC}$  electrocatalyst *via* *in situ* carburization of Mo-MOF under inert atmosphere, as shown in Scheme 1. The as-obtained catalyst is denoted as nanoMoC@GS, meaning highly dispersed and nanosized MoC encapsulated in graphitized carbon shell. In the



Scheme 1 Procedure for synthesis of nanoMoC@GS.

ordered porous architecture of the  $\text{Mo}_3(\text{BTC})_2$  precursor, the “atomic contact” between Mo ions and organic ligands enabled the formation of ultrafine MoC nanocrystallites ( $\sim 3$  nm), which were encapsulated by the fluffy and ultrathin graphitized carbon shell (*ca.* 1–3 layers). This confined geometry effectively inhibited the agglomeration and crystal growth of MoC nanocrystallites and, more importantly, resulted in improved conductivity and enriched porosity. The optimized nano-MoC@GS with a relatively low carburization temperature of 700 °C exhibited a robust and superior HER performance in both acidic and basic media, making it among the best performing among reported noble-metal-free electrocatalysts. This high HER activity is ascribed to the cooperative/synergistic effects of the ultrafine MoC nanoparticles, conductive and ultrathin graphitized carbon shells, and enriched porosity.

## Experimental

### Reagents

Trimesic acid ( $\text{H}_3\text{BTC}$ ), molybdenum hexacarbonyl ( $\text{Mo}(\text{CO})_6$ ), ethanol, sulfuric acid ( $\text{H}_2\text{SO}_4$ ) and potassium hydroxide (KOH) were purchased from Sinopharm Chemical Reagent Co., Ltd. (AR grade, China). Dimethylformamide (DMF), platinum on graphitized carbon (20 wt%) and Nafion® perfluorinated ion-exchange resin solution (5% w/w) were purchased from Sigma-Aldrich. All chemicals were used without further purification.

### Synthesis of porous and nanostructured molybdenum carbide

The  $\text{Mo}_3(\text{BTC})_2$  (Mo-MOF) were prepared according to the reported method.<sup>38</sup> In a typical synthesis, 1.13 g of  $\text{Mo}(\text{CO})_6$  and 0.75 g of  $\text{H}_3\text{BTC}$  were mixed with 50 mL of oxygen-free DMF. The resulting mixture was heated to reflux under argon at 155 °C under stirring for at least 5 days. After filtration and washing with oxygen-free DMF 3 times, the obtained orange-coloured precipitate was dried in vacuum at 135 °C. The *in situ* carburization process of  $\text{Mo}_3(\text{BTC})_2$  was conducted in a quartz tube under argon flow. After the precursor was packed in the tube, this tube was flushed with argon to expel air for 5 h at room temperature, the precursor was carburized at 700–900 °C for 5 h in an argon gas flow at a heating rate of 5 °C min<sup>-1</sup>, and then the tube was cooled to room temperature. The as-prepared catalysts were stored in a vacuum desiccator before use. The catalysts were labeled as nanoMoC@GS(*T*), in which *T* represents the carburization temperature. For example, the nano-MoC@GS(700) sample was obtained *via* *in situ* carburization of  $\text{Mo}_3(\text{BTC})_2$  at 700 °C under argon flow.

## Materials characterizations

The powder X-ray diffraction (XRD) patterns of the catalysts were recorded on a Bruker D8 Advance diffractometer with Cu K $\alpha$  radiation at 40 kV and 40 mA. The morphologies, structures and related element mapping information were obtained via field emission scanning electron microscopy (FESEM, Hitachi S-4800) and transmission electron microscopy (TEM, FEI Tecnai G2 F20 S-Twin), respectively. N<sub>2</sub>-sorption isotherms were collected on a Quantachrome Instruments Autosorb AS-6B adsorption analyzer at -196 °C. Brunauer–Emmett–Teller (BET) specific surface areas were calculated from adsorption data, and Barrett–Joyner–Halenda (BJH) pore size distribution was derived from the desorption branch of the isotherms. X-ray photoelectron spectroscopy (XPS) was collected on scanning X-ray microprobe (Thermo Scientific, ESCALAB 250Xi) using Al K $\alpha$  radiation and the C 1s peak at 284.8 eV as the internal standard. Raman spectra of powder samples were obtained on a laser confocal Raman microspectrometer (XploRA, Horiba Jobin Yvon, Ltd.) with a laser excitation wavelength of 532 nm.

## Electrochemical measurements

All electrochemical properties were evaluated with a standard three-electrode system using a CHI660E potentiostat (CH Instruments, China). A saturated calomel electrode (SCE) and a graphite rod were used as the reference electrode and counter electrode, respectively. The potential was converted to the potential *versus* the reversible hydrogen electrode (RHE) according to  $E(\text{RHE}) = E(\text{SCE}) + 0.2412 + 0.059\text{pH}$ . The working electrode was typically prepared *via* the following steps: (1) the as-prepared catalysts were dispersed in the solution containing 250  $\mu\text{L}$  of ethanol, 750  $\mu\text{L}$  of distilled water and 80  $\mu\text{L}$  of 5 wt% Nafion solution by ultrasonication for at least 1 h; (2) 4  $\mu\text{L}$  of the ink was loaded onto the surface of a glassy carbon electrode (GCE, 3.0 mm in diameter); and (3) the modified GCE was dried at room temperature. Before the data were recorded, the working electrode was cycled at least 50 times at a scan rate of 50 mV s<sup>-1</sup>. Linear sweep voltammetry (LSV) was recorded in 0.5 M H<sub>2</sub>SO<sub>4</sub> (pH = 0.3) and 1.0 M KOH (pH = 14) at a scan rate of 5 mV s<sup>-1</sup>. Long-term stability tests were performed by continuous linear sweep voltammetry scans at a sweep rate of 50 mV s<sup>-1</sup>. All data presented were corrected for iR losses throughout the system. Longer-term (10 h) stability was also tested under  $\eta = 150$  mV without iR correction in 0.5 M H<sub>2</sub>SO<sub>4</sub>. Cyclic voltammograms (CV) were obtained from 0 to 0.3 V (*versus* RHE, in 0.5 M H<sub>2</sub>SO<sub>4</sub>) and 0 to 0.3 (*versus* RHE, in 1.0 KOH) with sweep rates of 10, 25, 50, 75, 100, 150, 200, 250 and 300 mV s<sup>-1</sup>. Electrochemical impedance spectroscopy (EIS) was performed at various overpotentials with frequency from 0.01 to 10<sup>6</sup> Hz with an AC voltage of 5 mV.

## Results and discussion

### Characterization of porous and nanostructured nanoMoC@GS

First, the Mo<sub>3</sub>(BTC)<sub>2</sub> precursor (Mo-MOF) was synthesized, and its XRD pattern is given in Fig. S1.<sup>†</sup> The porous and

nanostructured nanoMoC@GS was then obtained by a simple *in situ* carburization of the as-prepared precursor under argon atmosphere. Fig. 1a shows the XRD patterns of the materials carburized at 700–900 °C. The sample carburized at 600 °C was not presented in this work, because this sample was so active that it would have self-ignited during its collection. Weaker and broader diffraction peaks indicated formation of nanocrystallites with very small size, which were ascribed to hexagonal  $\eta$ -MoC phase. Additionally, the diffraction peaks became stronger and sharper as carburization temperature increased, indicating greater crystallization and/or particle size of MoC. Interestingly, XRD patterns of the nanoMoC@GS gave results different from our previous researches, in which typically  $\beta$ -Mo<sub>2</sub>C was produced by pyrolyzing the MoO<sub>x</sub>/amine hybrid precursor at similar temperatures.<sup>13,25</sup> Mo *et al.* investigated the effect of carburization protocols on MoC<sub>x</sub> synthesis using a methanothermal temperature programmed reaction, and concluded that MoC formation was favored when a higher concentration of hydrocarbon or a long-chain hydrocarbon was used.<sup>39</sup> In this *in situ* carburization process, the organic ligands (BTC<sup>3-</sup>) of the MOF precursor played two different roles as they (1) removed the oxygen atom in the mixtures and (2) acted as a carbon source to form MoC<sub>x</sub>. Hence, the relatively higher C/Mo atomic ratio (6 : 1) and lower oxygen atom content in the MOF precursor contributed to MoC formation. Raman spectra were adopted to investigate the carbon state. The intensity ratio of the D to G band ( $I_D/I_G$ ) was normally used to evaluate the defect content of graphite/ene structures.<sup>40</sup> In Fig. 1b, the G bands located at *ca.* 1600 cm<sup>-1</sup> suggested formation of graphitized carbon in these materials, and similar  $I_D/I_G$ , 1.01 for nanoMoC@GS(700), 1.06 for nanoMoC@GS(800) and 1.02 for nanoMoC@GS(900), indicated that the carburization temperature in our experimental conditions had a slight influence on defects of the obtained graphite structure.

The morphology and detailed structure of the as-prepared nanoMoC@GS materials were investigated by SEM and TEM. Typically, nanoMoC@GS(700) (Fig. 2a) presented a morphology of stacked nanospheres with a smooth surface, suggesting that the MoC nanocrystallites (Fig. 2b) were surface covered by carbon species. The corresponding TEM images (Fig. 2c and d) also confirmed formation of the fluffy and ultrathin graphitized carbon shell (1–3 layers) in the sample, which encapsulated uniform and ultrafine nanocrystallites, as indicated by white arrows. This fluffy graphitized carbon shell and confined geometry have three main advantages: (1) enhancement of the

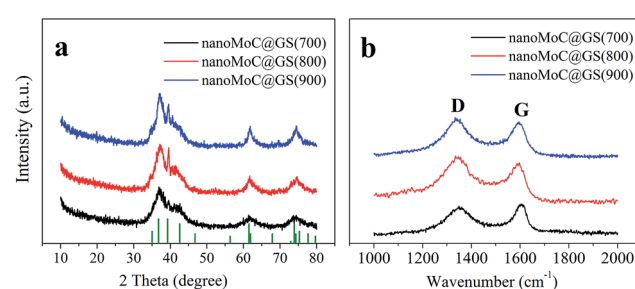


Fig. 1 XRD patterns (a) and Raman spectra (b) of nanoMoC@GS( $T$ ).

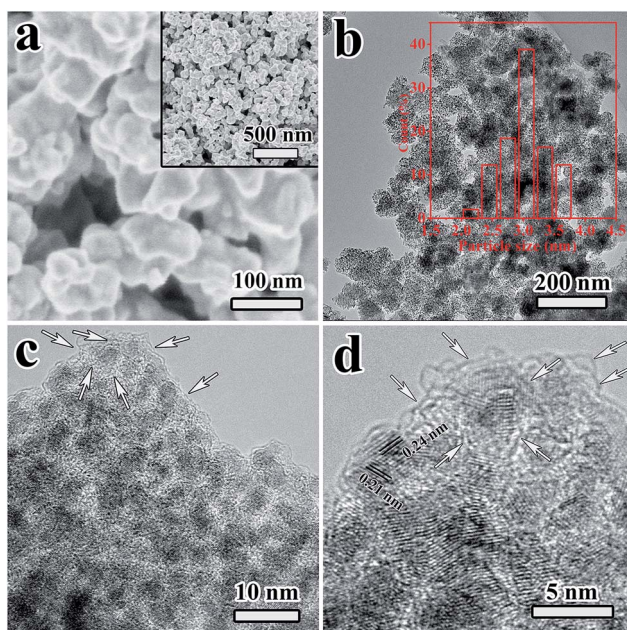


Fig. 2 SEM (a), TEM (b, c) and HRTEM (d) images of nanoMoC@GS(700).

interface contact of MoC nanoparticles with the lamellar graphitized carbon shell, which could suppress the dissolution or agglomeration of MoC nanoparticles, (2) improvement of the electrocatalyst conductivity, allowing rapid charge transfer kinetics during the electrochemical process, and (3) presentation of a very high surface area that not only exposes abundant special catalytic sites but also facilitates electrolyte access and diffusion of produced hydrogen. Notably, the size of as-prepared MoC nanocrystallites ( $\sim 3$  nm, Fig. 2b inset) *via* this “MOFs-directed strategy” was smaller and more even than that obtained *via* the “MOFs-assisted strategy” ( $\sim 5$  nm in size with some larger particles appearing at the corners<sup>15</sup>) and our previous “organic–inorganic hybrid-conversion strategy” (10–15 nm in size).<sup>13</sup> This ultrafine nanostructure was promoted by “atomic contact” between Mo ions and organic ligands in the ordered porous architecture of the Mo-MOF precursor that effectively prevented the coalescence and crystal growth of MoC nanocrystallites during carburization. The lattice fringes of 0.21 and 0.24 nm in high-resolution TEM (HRTEM, Fig. 2d) corresponded to the (103) and (006) planes of  $\eta$ -MoC, respectively. After increasing the carburization temperature, the agglomeration of MoC nanoparticles could be detected, resulting in larger particle size and broader distribution of MoC particles (Fig. S2†). Meanwhile, scanning transmission electron microscopy (STEM, Fig. 3a) and corresponding elemental mapping (Fig. 3b and c) showed that the Mo and C atoms were homogeneously distributed over the entire material, suggesting that MoC nanocrystals were evenly integrated within the graphitized carbon shell. The element composition of nanoMoC@GS(700) was studied *via* energy dispersive spectrometer (EDS, Fig. 3d). Contents of the graphitized carbon and Mo in the nano-MoC@GS were calculated and measured by TGA and ICP-AES, respectively, and the results are given in Fig. S3 and Table S1.† It

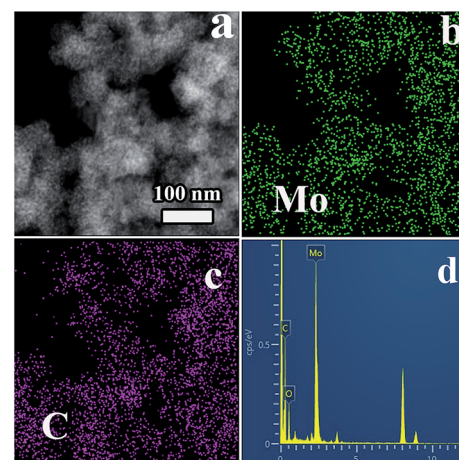
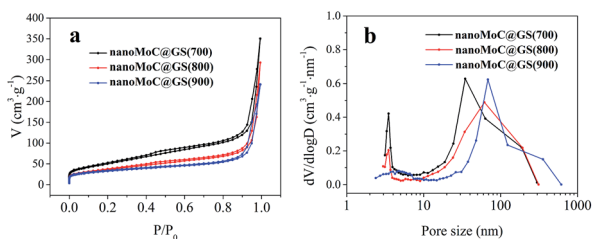


Fig. 3 STEM image (a), elemental mappings (b, c) and EDS spectrum (d) of nanoMoC@GS(700).

could be seen that the content of graphitized carbon decreased with increasing carburization temperature while that of MoC increased synchronously, which might result from removal of organic fragments in the graphite shell at higher treatment temperatures. Furthermore, these three samples were analysed by XPS (Fig. S4†). The peak fitting of Mo 3d profiles suggested that there had been four states (+2, +3, +4 and +6) for Mo on the surface. Mo<sup>4+</sup> and Mo<sup>6+</sup> species resulted from inactive MoO<sub>2</sub> and MoO<sub>3</sub>, respectively, which are commonly observed as carbides are exposed to air.<sup>12,22,37</sup> We focused on the Mo<sup>2+</sup> and Mo<sup>3+</sup> species peaking in 228.1–228.9 eV (Mo 3d<sub>5/2</sub>) and 231.3–232.0 eV (Mo 3d<sub>3/2</sub>), because they were the main species in MoC and the active centres for electrocatalytic HER.<sup>37</sup> The content of (Mo<sup>3+</sup> + Mo<sup>2+</sup>) and Mo<sup>3+</sup>/Mo<sup>2+</sup> mole ratios ( $n_{3+/2+}$ ) were applied to identify the properties of active sites for HER (Table S1†). It could be seen that the values above did not show obvious variation between the samples carburized at different temperatures with the same precursor, indicating similar composition and electronic environment of active sites in these samples. In addition, C 1s XPS profiles of the as-obtained nanoMoC@GS materials showed similar position and shape of peaks (Fig. S4b†). The peaks of C 1s narrowed with the increase in carburization temperature, which could probably be ascribed to removal of organic fragments in the graphite shell at higher treatment temperatures.

BET surface area and BJH pore size distribution were measured by N<sub>2</sub>-sorption isothermal analysis. As shown in Fig. 4a, the obtained nanoMoC@GS materials primarily inherited the enriched porosity of the Mo-MOF precursor after *in situ* carburization. A very high BET surface area ( $S_{\text{BET}} = 187 \text{ m}^2 \text{ g}^{-1}$ ) was achieved on the nanoMoC@GS(700) sample, which decreased to 131 and 115  $\text{m}^2 \text{ g}^{-1}$  as the carburization temperature increased to 800 and 900 °C, respectively. Meanwhile, a typical bimodal porosity was observed in the materials (Fig. 4b). The nanopores of 3–4 nm probably resulted from the fluffy graphitized carbon shell and/or aggregation of MoC nanocrystallites inside the materials (Fig. 2c and d), and the abundant meso/macropores distributed in the range of 20–300



**Fig. 4**  $N_2$ -sorption isotherms of nanoMoC@GS(7) (a) and corresponding pore size distribution curves (b) calculated from desorption branches.

nm were ascribed to the secondary piled pore of nanoMoC@GS particles (Fig. 2a), which did not appear in our previous  $Mo_2C$  nanowires obtained by pyrolyzing the  $MoO_x$ /amine hybrid precursor.<sup>13</sup> Herein, it was expected that high surface area and special meso/macropore structures would decrease the diffusion resistance and promote the exposure of active sites during the electrochemical process, resulting in improved HER performance in these materials.

### HER catalytic activities of nanoMoC@GS catalysts

The as-prepared nanoMoC@GS materials were studied as electrocatalysts for HER in 0.5 M  $H_2SO_4$ , and the HER activity of Pt/C (20 wt%) was also evaluated under the same conditions. The HER activity of nanoMoC@GS materials was first investigated with the mass loading of 0.76 mg  $cm^{-2}$ , which is similar to that of the previously reported  $MoC_x$  nano-octahedrons prepared *via* carburizing the Cu-MOF template with pre-embedded polyoxometalate guests.<sup>15</sup> Fig. 5a shows the HER activity of nanoMoC@GS prepared at three different carburization temperatures. NanoMoC@GS(700) exhibited optimal HER performance in acidic media, while those prepared at higher carburization temperatures showed slightly inferior performance. In particular, nanoMoC@GS(700) achieved

current densities of 1 and 10 mA  $cm^{-2}$  with lowest overpotentials of 84 ( $\eta_1$ ) and 132 mV ( $\eta_{10}$ ), respectively. Beyond this, the cathodic current density increased rapidly at more negative potentials with a very high current density ( $j_{200}$ ) of 100 mA  $cm^{-2}$  at an overpotential of 200 mV. Such excellent performances were even better than results reported by Lou and colleagues' work on  $MoC_x$  nano-octahedrons produced by the "MOFs-assisted strategy" from polyoxometalate-embedded Cu-MOF,<sup>15</sup> or our previous report on  $Mo_2C$  nanowires converted from  $Mo_3O_{10}(C_6H_8N)_2 \cdot 2H_2O$  hybrid precursor.<sup>13</sup> For example, the  $j_{200}$  value on our catalyst was about twice those of Lou and colleagues and our previous work ( $j_{200} = \sim 40$  and 60 mA  $cm^{-2}$ , respectively). Moreover, the smallest Tafel slope (46 mV  $dec^{-1}$ ) was also obtained for nanoMoC@GS(700), suggesting that the reaction proceeds through the Volmer–Heyrovsky mechanism in which the electrochemical desorption step was rate limiting.<sup>3,13</sup> By extrapolating the Tafel plot, the exchange current density ( $j_0$ ) of nanoMoC@GS(700) was calculated as  $13.5 \times 10^{-3}$  mA  $cm^{-2}$ , which was also much higher than that of the other two samples derived from higher temperatures (Table S2†), reflecting the lower reaction resistance in this former sample.

The electrochemical surface area (ECSA) is directly related to the HER activity, but its accurate measurement for  $MoC_x$  is difficult due to its unclear capacitive behavior.<sup>21,22</sup> Hence, the electrochemical double-layer capacitances ( $C_{dl}$ ) measured by the CV method (Fig. S5†) were widely applied to evaluate relative ECSA of the catalysts. As expected, given its highest HER activity, nanoMoC@GS(700) did show the largest  $C_{dl}$  value of 66.6 mF  $cm^{-2}$  (Fig. 5c), implying that this sample had a much higher ECSA than the samples prepared at higher carburization temperatures. Meanwhile, the surface area ( $S_{BET}$ ) of the samples followed the same decreasing order of the  $C_{dl}$  value with the increase in carburization temperature, that is, nanoMoC@GS(700) ( $187 \text{ m}^2 \text{ g}^{-1}$ ) > nanoMoC@GS(800) ( $131 \text{ m}^2 \text{ g}^{-1}$ ) > nanoMoC@GS(900) ( $115 \text{ m}^2 \text{ g}^{-1}$ ). It has been suggested that the  $S_{BET}$  was a crucial parameter for HER by enabling the rapid diffusion of species during the reactions.<sup>13,15,41</sup> In order to evaluate the contribution of  $S_{BET}$  to ESCA or HER activity, the  $C_{dl}/S_{BET}$  ratios were calculated: 0.37 for nanoMoC@GS(700), 0.32 for nanoMoC@GS(800), and 0.14 for nanoMoC@GS(900). Notably, this ratio decreased in turn rather than remaining unchanged in the samples with increasing carburization temperature, indicating that  $S_{BET}$  was not the sole cause affecting ECSA or HER activity. The XPS results have revealed that a similar composition and electronic environment of active sites existed in three samples. Therefore, this variation of  $C_{dl}/S_{BET}$  ratio was ascribed to other active-site structural disparity besides porosity and surface area. TEM images showed that increasing carburization temperature resulted in agglomeration of MoC nanoparticles, and the smallest and most uniform MoC nanocrystallites were obtained in nanoMoC@GS(700). Such special features of this catalyst with ultrafine MoC nanostructure supported on an exposed structure ensured proliferating active sites on its surface, thus contributing to the outstanding HER activity. Thus far, we lack a good technique for directly quantifying the amount of exposed  $\eta$ -MoC active sites and ECSA, and it is difficult to obtain the accurate turnover

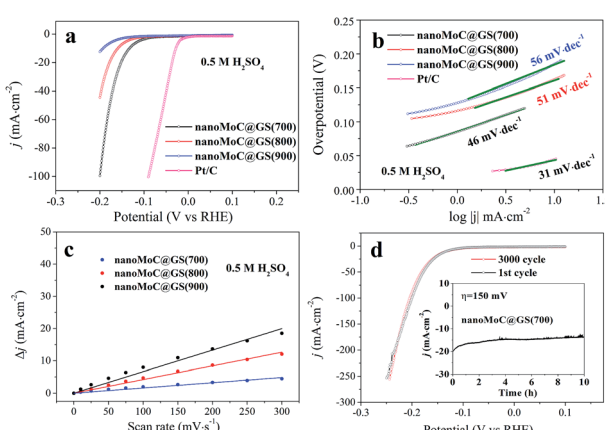


**Fig. 5** (a) Polarization curves for the three catalysts. (b) Corresponding Tafel plots. (d) Capacitive current at 0.15 V as function of scan rate. (c) Durability measurements with nanoMoC@GS(700). Inset: time dependence of catalytic currents during electrolysis for nanoMoC@GS(700) in 0.5 M  $H_2SO_4$  at  $\eta = 150$  mV.

frequency (TOF) of the electrocatalysts. Alternatively, the ratios of  $j_{200}$  to  $C_{dl}$  of the three samples were adopted to estimate the relative TOFs of the various nanoMoC@GS due to the proportional relationship of  $C_{dl}$  value to ECSA. The values were 1.5 for nanoMoC@GS(700), 1.1 for nanoMoC@GS(800), and 0.8 for nanoMoC@GS(900). This result indicated declining intrinsic activity of the active sites in the sample carburized at higher temperature, which was quite consistent with the variety of  $C_{dl}/S_{BET}$  ratios. It also confirmed the existence of cooperative/synergistic effects of ultrafine MoC and the catalyst's open structure.

The experiment for long-term stability of nano-MoC@GS(700) (Fig. 5d) showed only a little deterioration of cathodic currents after 3000 cycles. Meanwhile, the result of chronoamperometry (CA) for nanoMoC@GS(700) showed that the catalytic currents remained at around  $15 \text{ mA cm}^{-2}$  at 150 mV over 10 h, demonstrating the high stability under experimental conditions employed for this HER process. The HRTEM images of nanoMoC@GS(700) after electrochemical stability testing are provided in Fig. S6.<sup>†</sup> NanoMoC@GS(700) structure and particle size distribution of the MoC nanoparticles showed only slight changes, confirming the superior stability of this electrocatalyst, which resulted from the confined geometry (ultrafine MoC nanoparticles encapsulated by graphitized carbon shells) in this material.

We then used EIS to provide further insight into electrode kinetics of the obtained materials. As shown in Fig. 6a, nano-MoC@GS(700) presented a much lower charge-transfer resistance ( $R_{ct}$ ) value ( $14.5 \Omega$ ) than nanoMoC@GS(800) ( $28.6 \Omega$ ) and nanoMoC@GS(900) ( $69.5 \Omega$ ), indicating a faster electron transfer rate in the HER process. This lower  $R_{ct}$  should be related to the confined geometry in nanoMoC@GS materials, which would enhance the close interface contract of MoC nanoparticles with the ultrathin graphitized carbon shell and allow rapid charge transfer kinetics during the electrochemical process by improving the conductivity of electrocatalysts. The lowest  $R_{ct}$  value for nanoMoC@GS(700) might result from its relatively large quantity of graphitized carbon (Table S1<sup>†</sup>). EIS for nanoMoC@GS(700) at various HER overpotentials from 75 to 200 mV in 0.5 M H<sub>2</sub>SO<sub>4</sub> is provided in Fig. S7.<sup>†</sup> The

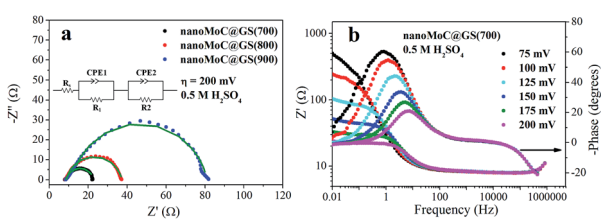


Fig. 6 (a) EIS for the three samples. Data are fitted to simplified equivalent circuit shown in inset, and fitting results are plotted as solid traces. In the equivalent circuit model for electrochemical impedance tests,  $R_s$ ,  $R_1$  and  $R_2$  represent the electrolyte, electrode porosity and charge transfer resistance, respectively. CPE is the constant phase angle element, which represents double-layer capacitance of solid electrode in the real-world situation. (b) Nyquist and Bode plots showing EIS responses of nanoMoC@GS(700) sample at various HER overpotentials in 0.5 M H<sub>2</sub>SO<sub>4</sub>.

corresponding Nyquist and Bode plots of the EIS response of nanoMoC@GS(700) are given in Fig. 6b, and two peaks could be detected in the curves. The first one with potential-dependent properties at low frequencies could be attributed to kinetics of the HER process; while another at high frequencies with the same intensity suggested that this electrocatalyst processed an abundant porosity,<sup>13</sup> which was in agreement with N<sub>2</sub>-sorption experimental results.

It has been widely demonstrated that different electrocatalysts have varying optimal mass loadings for HER.<sup>15,16,20</sup> The optimal mass loading of nanoMoC@GS(700) was also investigated. Results (Fig. 7a) showed that the optimal mass loading was  $1.04 \text{ mg cm}^{-2}$ . The lower overpotentials of 77 for  $\eta_1$  and 124 mV for  $\eta_{10}$  could be achieved at this point. The  $j_{200}$  at the higher overpotential of 200 mV was up to  $146 \text{ mA cm}^{-2}$  with a smaller Tafel slope of  $43 \text{ mV dec}^{-1}$  (Fig. S8<sup>†</sup>) and a larger  $j_0$  of  $15.1 \times 10^{-3} \text{ mA cm}^{-2}$ . Fig. 7b depicts relationships among mass loadings with current density at overpotentials of 150 and 200 mV, and two individual volcano curves could be observed. Notably, in the range from 0.16 to  $1.04 \text{ mg cm}^{-2}$ , current density linearly increased along with mass loading, indicating that the material's active sites would not overlap under such a large mass loading and that the HER activity was dominated by the active site number. This result was likely attributable to not only enriched meso/macropores structures but also nanostructure and graphitized carbon shells, which would completely expose active sites with excellent conductivity and very fast diffusion of electrolytes and H<sub>2</sub> under such a high mass loading on the electrode surface. Additionally, to the best of our knowledge, the HER activity of nanoMoC@GS(700) characterized by low  $\eta_{10}$  (124 mV), high  $j_{200}$  ( $146 \text{ mA cm}^{-2}$ ) and striking kinetic metrics ( $b = 43 \text{ mV dec}^{-1}$ ), which performed among the best of current noble metal-free electrocatalysts in acidic media (Table S3<sup>†</sup>). In the case of metal carbides, the  $\eta_{10}$  of 124 mV on nano-MoC@GS(700) was lower than that of reported Mo<sub>2</sub>C nanowires (130 mV),<sup>13</sup> MoC<sub>x</sub> nano-octahedrons (142 mV),<sup>15</sup> MoC–Mo<sub>2</sub>C heteronanowires (126 mV),<sup>26</sup> Mo<sub>2</sub>C nanotubes (172 mV),<sup>42</sup> and even supported MoC<sub>x</sub> (Mo<sub>2</sub>C/N-doped CNT: 147 mV; Mo<sub>2</sub>C/RGO: 150 mV; Mo<sub>2</sub>C/CNT: 152 mV). Although better activity has been achieved on MoC<sub>x</sub> catalysts,<sup>3,17,19,21</sup> they usually require secondary component modifications, such as doping an element (N, P, etc.) and/or conductive supports (RGO, CNT, etc.) e.g., N-doping Mo<sub>2</sub>C@carbon ( $\eta_{10} = 78 \text{ mV}$ )<sup>22</sup> and Mo<sub>2</sub>C–Mo<sub>2</sub>N–RGO ( $\eta_{10} = 109 \text{ mV}$ ).<sup>14</sup> The high HER performance of Nano-MoC@GS(700) without secondary modifications suggested this

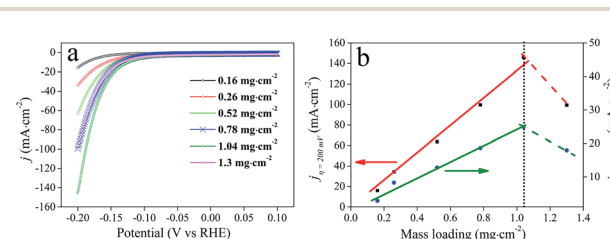
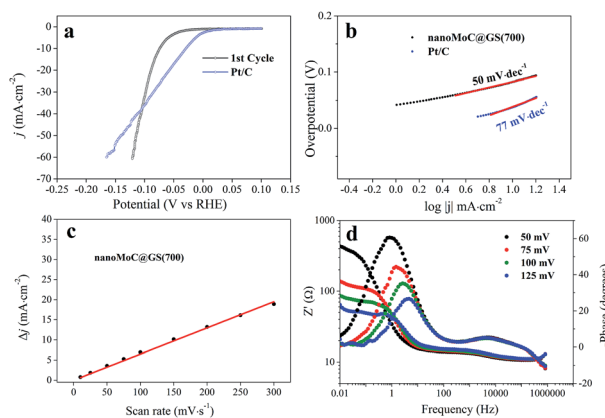


Fig. 7 (a) Polarization curves of nanoMoC@GS(700) catalyst under different mass loadings. (b) Relationships between mass loadings with current density at overpotential of 200 and 150 mV in 0.5 M H<sub>2</sub>SO<sub>4</sub>.



**Fig. 8** (a) Polarization curves for nanoMoC@GS(700) sample in 1.0 M KOH. (b) Corresponding Tafel plots. (c) Capacitive current at 0.15 V as a function of scan rate. (d) Nyquist and Bode plots showing EIS responses of nanoMoC@GS(700) sample at various HER overpotentials in 1.0 M KOH.

catalyst's superiority and possibilities for further improvement of its HER activity.

In order to expand the application range of this material, HER activity of the nanoMoC@GS(700) sample was also evaluated in basic media with the comparable mass loading of 0.76 mg cm<sup>-2</sup>; results are depicted in Fig. 8. The nanoMoC@GS(700) also exhibited super HER activity in basic media with an ultra-small  $\eta_1$  (42 mV) and  $\eta_{10}$  (77 mV), respectively. Meanwhile, it exhibited large  $C_{dl}$  values of 64.9 mF cm<sup>-2</sup> (Fig. 8c and S9†) and a small  $R_{ct}$  of 34.8 (Fig. S10†) at 125 mV, suggesting that this electrocatalyst also possessed a large ECSA and faster electron transfer rates in basic media. Notably, Pt/C showed an overwhelming advantage in acidic media, while the HER activity of nanoMoC@GS(700) even exceeded that of Pt/C at the high overpotential (>125 mV) in basic media. This interesting result was ascribed to different reaction pathways for the two catalysts, which were reflected by the different Tafel slope (77 mV dec<sup>-1</sup> for Pt/C and 50 mV dec<sup>-1</sup> for nanoMoC@GS) in Fig. 8b.<sup>15</sup> Additionally, the Nyquist and Bode plots of the EIS response for nanoMoC@GS(700) were depicted in Fig. 8d, and the peak at high frequencies also demonstrated the enriched porosity of this catalyst. Such prominent HER activity of nanoMoC@GS(700) in basic media was almost the best among the current noble metal-free HER electrocatalysts (Table S5†). Overall these results clearly indicated that nanoMoC@GS(700) is a highly versatile, efficient HER electrocatalyst over a wide pH range.

## Conclusion

In summary, we have developed a “MOFs-directed strategy” to synthesize porous nanoMoC@GS with ultrafine MoC nanoparticles confined in graphitized carbon shell for efficient HER. The nanoMoC@GS was prepared by simple *in situ* carburizing Mo-MOF under an inert atmosphere. This ultrafine nanostructure was ascribed to the real “atomic contact” between the Mo ions and organic ligands in the ordered porous architecture

of the MOF precursor. The obtained electrocatalyst showed the following: (1) the MoC nanocrystallites (~3 nm in size) were embedded in conductively ultrathin graphitized carbon shells (*ca.* 1–3 layers), which would prevent excess growth and coalescence during the carburization and usage process; and (2) enhanced conductivity and enriched porosity were achieved by this confined geometry and fluffy graphitized carbon shells. Benefiting from the cooperative/synergistic effects of ultrafine MoC nanostructure, ultrathin graphitized carbon shells and enriched porosity, the nanoMoC@GS material exhibited remarkable electrocatalytic activity for HER in both acidic and basic media with good stability, performing among the best of the current noble-metal-free electrocatalysts. The  $\eta_{10}$  of 124 and 77 mV, Tafel slope of 43 and 50 mV dec<sup>-1</sup>, and  $j_0$  of 0.015 and 0.212 mA cm<sup>-2</sup> was observed on the optimized nanoMoC@GS(700) sample in 0.5 M H<sub>2</sub>SO<sub>4</sub> and 1.0 M KOH, respectively. In addition, this strategy not only enriched the applications of MOFs to synthesize various functional materials, but also opened up new opportunities to develop nanocatalysts in the energy chemistry field.

## Acknowledgements

This work is supported by the National Key Basic Research Program of China (2013CB934101), NSFC (21433002, 21373102, 21573046), Sinopec (X514005), China Postdoctoral Science Foundation (2015M580289) and National Plan for Science and Technology of Saudi Arabia (14-PET827-02). Q. S. Gao is also grateful for support from the Natural Science Foundation of Guangdong Province (2015A030306014 and 2014TQ01N036) and Guangdong Higher Education Institute (YQ2013022).

## Notes and references

- J. Yang, A. Sudik, C. Wolverton and D. J. Siegel, *Chem. Soc. Rev.*, 2010, **39**, 656.
- B. Sakintuna, F. Lamari-Darkrim and M. Hirscher, *Int. J. Hydrogen Energy*, 2007, **32**, 1121.
- C. G. Morales-Guio, L.-A. Stern and X. Hu, *Chem. Soc. Rev.*, 2014, **43**, 6555.
- W. F. Chen, J. T. Muckerman and E. Fujita, *Chem. Commun.*, 2013, **49**, 8896.
- P. C. Vesborg, B. Seger and I. Chorkendorff, *J. Phys. Chem. Lett.*, 2015, **6**, 951.
- H. Lv, Z. Xi, Z. Chen, S. Guo, Y. Yu, W. Zhu, Q. Li, X. Zhang, M. Pan, G. Lu, S. Mu and S. Sun, *J. Am. Chem. Soc.*, 2015, **137**, 5859.
- T. Yang, M. Du, H. Zhu, M. Zhang and M. Zou, *Electrochim. Acta*, 2015, **167**, 48.
- Y. Zheng, Y. Jiao, Y. Zhu, L. H. Li, Y. Han, Y. Chen, A. Du, M. Jaroniec and S. Z. Qiao, *Nat. Commun.*, 2014, **5**, 3783.
- L. Gan, T. L. Groy, P. Tarakeshwar, S. K. Mazinani, J. Shearer, V. Mujica and A. K. Jones, *J. Am. Chem. Soc.*, 2015, **137**, 1109.
- R. Wu, J. Zhang, Y. Shi, D. Liu and B. Zhang, *J. Am. Chem. Soc.*, 2015, **137**, 6983.

- 11 J. S. Qin, D. Y. Du, W. Guan, X. J. Bo, Y. Li, L. Guo, Z. M. Su, Y. Y. Wang, Y. Q. Lan and H. C. Zhou, *J. Am. Chem. Soc.*, 2015, **137**, 7169.
- 12 H. Vrubel and X. Hu, *Angew. Chem.*, 2012, **124**, 12875.
- 13 L. Liao, S. N. Wang, J. J. Xiao, X. J. Bian, Y. H. Zhang, M. D. Scanlon, X. L. Hu, Y. Tang, B. H. Liu and H. H. Girault, *Energy Environ. Sci.*, 2014, **7**, 387.
- 14 W. F. Chen, S. Iyer, S. Iyer, K. Sasaki, C. H. Wang, Y. Zhu, J. T. Muckerman and E. Fujita, *Energy Environ. Sci.*, 2013, **6**, 1818.
- 15 H. B. Wu, B. Y. Xia, L. Yu, X. Y. Yu and X. W. D. Lou, *Nat. Commun.*, 2015, **6**, 6512.
- 16 C. He and J. Tao, *Chem. Commun.*, 2015, **51**, 8323.
- 17 Z. Y. Wu, X. X. Xu, B. C. Hu, H. W. Liang, Y. Lin, L. F. Chen and S. H. Yu, *Angew. Chem.*, 2015, **127**, 8297.
- 18 D. H. Youn, S. Han, J. Y. Kim, J. Y. Kim, H. Park, S. H. Choi and J. S. Lee, *ACS Nano*, 2014, **8**, 5164.
- 19 K. Xiong, L. Li, L. Zhang, W. Ding, L. Peng, Y. Wang, S. Chen, S. Tan and Z. Wei, *J. Mater. Chem. A*, 2015, **3**, 1863.
- 20 W. Cui, N. Cheng, Q. Liu, C. Ge, A. M. Asiri and X. Sun, *ACS Catal.*, 2014, **4**, 2658.
- 21 Y. Liu, G. Yu, G. D. Li, Y. Sun, T. Asefa, W. Chen and X. Zou, *Angew. Chem., Int. Ed.*, 2015, **54**, 10752.
- 22 R. Ma, Y. Zhou, Y. Chen, P. Li, Q. Liu and J. Wang, *Angew. Chem., Int. Ed.*, 2015, **54**, 14723.
- 23 W. F. Chen, C. H. Wang, K. Sasaki, N. Marinkovic, W. Xu, J. Muckerman, Y. Zhu and R. Adzic, *Energy Environ. Sci.*, 2013, **6**, 943.
- 24 Q. S. Gao, S. N. Wang, H. C. Fang, J. W. Weng, Y. H. Zhang, J. J. Mao and Y. Tang, *J. Mater. Chem.*, 2012, **22**, 4709.
- 25 Q. S. Gao, C. X. Zhang, S. H. Xie, W. M. Hua, Y. H. Zhang, N. Ren, H. L. Xu and Y. Tang, *Chem. Mater.*, 2009, **21**, 5560.
- 26 H. L. Lin, Z. P. Shi, S. N. He, X. Yu, S. N. Wang, Q. S. Gao and Y. Tang, *Chem. Sci.*, 2016, DOI: 10.1039/c6sc00077k.
- 27 V. Di Noto, E. Negro, S. Polizzi, F. Agresti and G. A. Giffin, *ChemSusChem*, 2012, **5**, 2451–2459.
- 28 E. Negro, S. Polizzi, K. Vezzù, L. Toniolo, G. Cavinato and V. Di Noto, *Int. J. Hydrogen Energy*, 2014, **39**, 2828.
- 29 V. Di Noto, E. Negro, S. Polizzi, K. Vezzù, L. Toniolo and G. Cavinato, *Int. J. Hydrogen Energy*, 2014, **39**, 2812.
- 30 E. Negro, K. Vezzù, F. Bertasi, P. Schiavuta, L. Toniolo, S. Polizzi and V. Di Noto, *ChemElectroChem*, 2014, **1**, 1359.
- 31 H. C. Zhou and S. Kitagawa, *Chem. Soc. Rev.*, 2014, **43**, 5415.
- 32 H. C. Zhou, J. R. Long and O. M. Yaghi, *Chem. Rev.*, 2012, **112**, 673.
- 33 R. R. Salunkhe, J. Tang, Y. Kamachi, T. Nakato, J. H. Kim and Y. Yamauchi, *ACS Nano*, 2015, **9**, 6288.
- 34 X. Xu, R. Cao, S. Jeong and J. Cho, *Nano Lett.*, 2012, **12**, 4988.
- 35 S. J. Yang, S. Nam, T. Kim, J. H. Im, H. Jung, J. H. Kang, S. Wi, B. Park and C. R. Park, *J. Am. Chem. Soc.*, 2013, **135**, 7394.
- 36 H. L. Jiang, B. Liu, Y. Q. Lan, K. Kuratani, T. Akita, H. Shioyama, F. Zong and Q. Xu, *J. Am. Chem. Soc.*, 2011, **133**, 11854.
- 37 C. Wan, Y. N. Regmi and B. M. Leonard, *Angew. Chem.*, 2014, **126**, 6525.
- 38 M. Kramer, U. Schwarz and S. Kaskel, *J. Mater. Chem.*, 2006, **16**, 2245.
- 39 T. Mo, J. Xu, Y. Yang and Y. Li, *Catal. Today*, 2016, **261**, 101.
- 40 M. Xiao, J. Zhu, L. Feng, C. Liu and W. Xing, *Adv. Mater.*, 2015, **27**, 2521.
- 41 Y. J. Tang, M. R. Gao, C. H. Liu, S. L. Li, H. L. Jiang, Y. Q. Lan, M. Han and S. H. Yu, *Angew. Chem., Int. Ed.*, 2015, **54**, 12928.
- 42 F. X. Ma, H. B. Wu, B. Y. Xia, C. Y. Xu and X. W. D. Lou, *Angew. Chem., Int. Ed.*, 2015, **54**, 15395.